nature climate change

Article

https://doi.org/10.1038/s41558-025-02364-4

Rapid increases in satellite-observed ice sheet surface meltwater production

Received: 4 May 2024

Accepted: 27 May 2025

Published online: 04 July 2025

Check for updates

Lei Zheng[1,2], Xinyi Shang[3], Michiel R. van den Broeke[4], Brice Noël[5], Xichen Li[6], Xavier Fettweis[5], Qi Liang[1,2], Kang Wang[7], Jiping Liu[8] & Xiao Cheng[1,2]

Surface meltwater production influences the contribution of ice sheets to global sea-level change. Ice-sheet-wide meltwater production has thus far primarily been quantified by regional climate models. Here we present a 31-year (1992–2023) time series of daily satellite-observed surface melt flux for the Greenland and Antarctic ice sheets. The annual meltwater volume in Greenland has significantly increased, with intensified melt in the northern basins dominated by a negative North Atlantic Oscillation and elevated melt flux in western basins driven by the decline in Arctic sea-ice. In East Antarctica, high melt rates since 2000 are attributed to warm air incursions from the Southern Ocean due to anomalous atmospheric circulations associated with a negative Southern Annular Mode and the recovery of the Antarctic ozone hole. This region, previously less prone to surface melt, has become a melt hotspot, potentially leading to meltwater ponding and future ice shelf destabilization.

Polar ice sheet mass loss is one of the primary components of accelerated global sea-level rise over the past decades[1,2] and the rate of mass loss is more than three times higher today compared to the early 1990s[3]. Surface meltwater strongly affects the energy and mass balance through the snowmelt–albedo feedback[4,5], leading to surface lowering both in the Greenland ice sheet (GrIS) and Greenland peripheral glaciers[6,7]. Ice sheet volume and mass loss have been further amplified by the melt–elevation feedback and the exposure of dark, bare ice[8,9]. Meltwater drainage and the inland migration of the surface hydrology system enhance the link between surface melt and sea-level rise[10–12]. Surface meltwater can also fill and propagate fractures downwards through Greenland's remaining ice shelves[13,14]. Surface-to-bed meltwater connection on grounded ice can modulate both short- and long-term ice dynamics by altering the basal lubrication[15–19].

While most of the surface meltwater refreezes in the snowpack in the cold Antarctic climate[20,21], the melting process can still indirectly affect ice dynamics and mass balance of the Antarctic ice sheet (AIS). Ponded water and slush have been widely observed on low-lying ice shelves, where meltwater accumulation and drainage processes can cause ice shelf flexure[22–24]. Water-filled ice fractures may propagate vertically causing hydrofracture[25,26] and even result in ice shelf break-ups[27–30], leading to the acceleration of grounded ice discharge[31,32]. The AIS surface melt rate is projected to increase nonlinearly as the climate warms[33] and may become comparable to that of the present-day GrIS[34].

Continent-wide ice sheet surface melt has been studied using satellites[35–39] and regional climate models (RCMs)[20,40–42]. The reliability of modelled melt depends heavily on the quality and quantity of input parameters and physics parameterizations, and is challenging to evaluate owing to the difficulty and scarcity of direct observations[43,44].

[1]School of Geospatial Engineering and Science, Sun Yat-sen University and Southern Marine Science and Engineering Guangdong Laboratory (Zhuhai), Zhuhai, China. [2]Key Laboratory of Comprehensive Observation of Polar Environment (Sun Yat-sen University), Ministry of Education, Zhuhai, China. [3]Faculty of Geographical Science, Beijing Normal University, Beijing, China. [4]Institute for Marine and Atmospheric Research, Utrecht University, Utrecht, the Netherlands. [5]Laboratory of Climatology, Department of Geography, SPHERES Research Unit, University of Liège, Liège, Belgium. [6]Institute of Atmospheric Physics, Chinese Academy of Sciences, Beijing, China. [7]School of Geographic Sciences, East China Normal University, Shanghai, China. [8]School of Atmospheric Sciences, Sun Yat-sen University and Southern Marine Science and Engineering Guangdong Laboratory (Zhuhai), Zhuhai, China. e-mail: chengxiao9@mail.sysu.edu.cn

https://doi.org/10.1038/s41558-025-02364-4

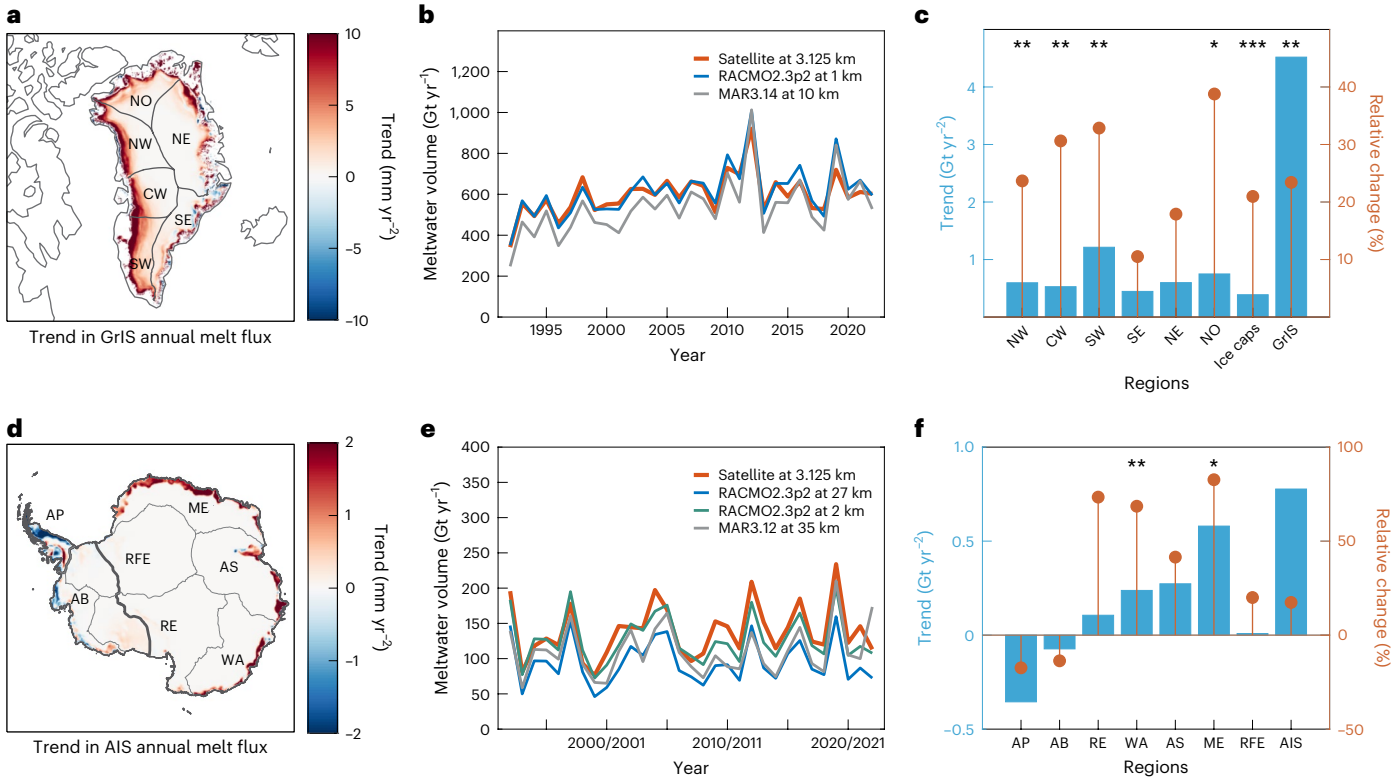

Fig. 1 | Satellite-derived dynamics of surface melt flux and meltwater volume. **a**,**d**, Maps of the trends in annual melt flux (mm yr^{-2}) over the GrIS (**a**) and AIS (**d**) between 1992 and 2022/2023 (n = 31). GrIS basins and ice caps in **a**, including North (NO), North-East (NE), South-East (SE), South-West (SW), Centre-West (CW) and North-West (NW) are adopted from Rignot and Mouginot[72]. AIS basins in **d**, including the Antarctic Peninsula (AP), Ronne-Filchner Embayment (RFE), Maud and Enderby (ME), Amery and Shackleton (AS), Wilkes and Adélie (WA), Ross Embayment (RE) and Amundsen Bellinghausen (AB), are adopted from Zwally et al.[73]. Thick black lines in **d** show the boundaries between the Antarctic Peninsula, West Antarctica and East Antarctica, referring to Zwally et al.[73]. **b**,**e**, Time series of annual meltwater volume of GrIS (**b**) and AIS (**e**) from satellite estimates and regional climate model simulations. **c**,**f**, Trends and relative changes (referenced to the annual average for each region) in meltwater volume over the GrIS (**c**) and AIS (**f**). Black stars in **c** and **f** indicate the trends are significant at 90% (*), 95% (**) and 99% (***) confidence levels (two-tailed t-test).

Spaceborne microwave observations are very sensitive to the snow liquid water[45–47], but only provide information on the presence/absence of meltwater rather than melt flux (the rate at which ice converts into water). Recently, Zheng et al.[48] developed a method to estimate daily surface melt flux over the GrIS from space, but this method was applied only to a single radiometer.

Here we use an established melt flux retrieval model for the GrIS[48] and develop a similar model for the AIS by leveraging machine learning to relate satellite observations to in situ melt flux. A 31-year time series of ice sheet daily melt flux is estimated at 3.125 km resolution by intercalibrating the earlier spaceborne radiometers from 1992 to 2022/2023 (Supplementary Text 1 and Extended Data Fig. 1). This dataset provides a benchmark for RCM evaluation, with satellite estimates aligning closely with outputs from RCMs over the GrIS, but trending higher over the AIS (Supplementary Text 2). The satellite estimates also enable an examination of changes in ice sheet meltwater production (the total amount of ice that transforms into water) under a changing climate.

Rapid increases in ice sheet meltwater production

Satellite-derived datasets indicate an intensification of GrIS surface melt concentrated in the ablation zone, particularly in the northern and western basins where the annual melt flux has increased at a rate >10 mm water equivalent (w.e.) yr^{-2} (Fig. 1a). During the period between 1992 and 2022, an average of 598 ± 101 Gt (mean ± s.d.) of meltwater was produced on the GrIS in each year. We analyse the trend and the relative change referenced to the annual average over the study period. Satellites observed a significant increase (P < 0.05) in GrIS annual meltwater volume over the 1992–2022 period with a rate of 4.5 ± 3.9 Gt yr^{-2} (in total 23% of the annual average) (Fig. 1b,c). The main contribution to the increase of GrIS meltwater occurred during July and August (Extended Data Fig. 2). Over the period, the strongest increases occurred at 1,100 m above sea level (Extended Data Fig. 3). Regionally, meltwater production increased in all GrIS basins, especially in the North Basin, where surface melt had increased at a rate of 0.75 ± 0.68 Gt yr^{-2} (Fig. 1c), representing a total relative increase of 39% compared to the annual average over the 1992–2022 period. Significantly positive trends were found in all the western basins, and the South-West Basin showed the most rapid increase (1.21 ± 1.01 Gt yr^{-2}, P < 0.05).

The meltwater volume produced by the AIS (139 ± 38 Gt yr^{-1}) was nearly one-quarter of that produced by the GrIS, with high interannual variability during 1992 to 2023 (Fig. 1). A substantial increase in annual melt flux was observed in East Antarctica, while a decline in surface melt occurred in the Antarctic Peninsula and the Amundsen Sea sector (Fig. 1d,f). For the full ice sheet, no significant trend (0.78 ± 1.56 Gt yr^{-2}) in meltwater production was observed in the satellite data during 1992 to 2023 (Fig. 1e,f). The satellite product did reveal evidence of significant increases in surface melt in Dronning Maud Land and Enderby Land (P < 0.1) and Wilkes Land and Adélie Land (P < 0.05), with a relative change of >70%. Overall, the East Antarctic annual meltwater volume has increased by 64% at a rate of 1.13 ± 1.13 Gt yr^{-2} (P = 0.05), with record high melt in the 2010s (Extended Data Fig. 4a). Only 26% of AIS meltwater was produced in East Antarctica during the 1992–2000 period, increasing to 45% during 2000 to 2023 (Extended Data Fig. 4b). As a result, East Antarctica has surpassed the Antarctic Peninsula as the primary contributor to AIS meltwater production.

https://doi.org/10.1038/s41558-025-02364-4

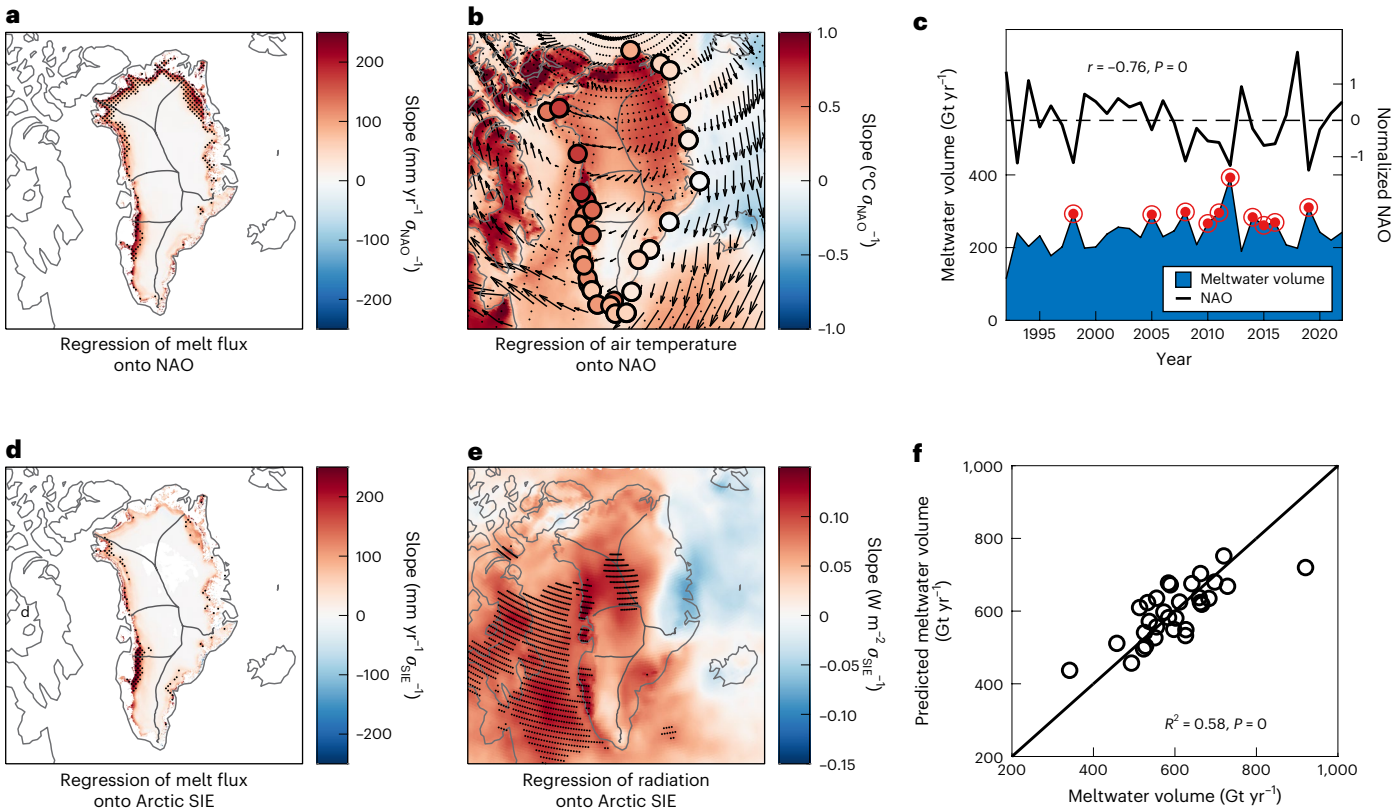

Fig. 2 | Climatic drivers of changes in GrIS surface melt. a, GrIS annual melt flux regressed on summer NAO. σ_{NAO} denotes one standard deviation of the NAO index. **b**, Summer air temperature and wind field regressed on summer NAO. Coloured dots represent temperature anomalies recorded by stations from the Danish Meteorological Institute[74]. **c**, Comparison between North GrIS annual meltwater volume and summer NAO. Red circles indicate the ten highest North GrIS meltwater production records. **d**, GrIS annual melt flux regressed on summer Arctic SIE[75]. σ_{SIE} denotes one standard deviation of the Arctic SIE. **e**, ERA5 (ref. 76) downward long-wave radiation regressed on summer Arctic SIE. **f**, Scatterplot showing the comparison between GrIS meltwater volume observed from satellite and that predicted by summer NAO and Arctic SIE based on multiple linear regression. Note that the signs of NAO and SIE are reversed. Black dots in **a**, **b**, **d** and **e** indicate the correlations are significantly at a 99% confidence level (two-tailed *t*-test). Black lines in **a**, **b**, **d** and **e** show the basin boundaries[72].

Climatic drivers of increased Greenland meltwater production

Our satellite-derived results show that an increase in surface meltwater volume in Greenland occurred during the 1992–2022 period, particularly in the northern and western basins. Our study confirms a significant correlation between GrIS annual meltwater volume and the North Atlantic Oscillation (NAO) ($r = -0.67$, $P < 0.01$), which has been previously documented[49]. This correlation is much stronger than that between surface melt and the increasing global temperature ($r = 0.28$) (Extended Data Fig. 5a). Greenland meltwater production shows a close relationship ($r = 0.76$) with the Greenland Blocking Index (Extended Data Fig. 5a). Associated with the negative NAO, a higher frequency of high-pressure blocking events promoted the advection of warm air masses towards the ice sheet during years of extreme melt[50,51]. Regression analysis based on detrended time series further confirms that the NAO has exerted a dominant influence on surface melt flux in North GrIS (including NW, NO and NE basins) (Fig. 2a). The map of summer air temperature and wind field anomalies regressed onto the NAO shows that the warming and ocean air incursion in the North GrIS occurred with a negative NAO (Fig. 2b). This explains why the ten highest melt seasons in the North GrIS were all accompanied by a negative NAO and the meltwater–NAO correlation reached −0.76 ($P < 0.01$) during the study period (Fig. 2c).

The regression of detrended summer Arctic sea-ice extent (SIE) to GrIS surface melt flux confirms the decline in Arctic sea-ice is a key driver of the enhanced GrIS surface melt (Fig. 2d), due to a warmer and more humid atmosphere[52]. We found the relationship was especially strong and significant in the ablation zone of the western GrIS, where the downward long-wave radiation was strongly linked to the decline in Arctic SIE (Fig. 2e). A singular value decomposition analysis reveals an extensive connection between increasing melt flux in the western GrIS and decline of summer sea-ice in Baffin Bay (55–75° N, 75–50° W) where the most rapid decline in sea-ice over the past few decades has been observed[53] (Extended Data Fig. 6). The expansion coefficient of the leading singular value decomposition mode for the Baffin Bay sea-ice concentration shows a significant anti-correlation with detrended western GrIS meltwater volume ($r = -0.72$, $P < 0.01$).

Summer NAO and Arctic SIE together explained 58% of the GrIS meltwater volume variations (Fig. 2f). Surface melt in North GrIS shows the highest correlation with NAO, possibly due to the increased high-amplitude omega blocks in summer, which produced more melt across northern basins[54]. Meltwater volume in western Greenland exhibits a high correlation to the reduction of Arctic sea-ice, which facilitates the inland transport of warm marine air and has been shown to lead to an expansion of the melt area and an earlier onset of melt[55,56]. Our satellite-based product reveals especially large changes in meltwater volume in the elevation range of 1,000–1,800 m (Extended Data Fig. 3), where the equilibrium line is typically located. This can potentially result in the extension of the GrIS ablation (summer bare ice) area and the inland migration of supraglacial lakes[10], which can in turn amplify surface melt and ice sheet mass loss through the positive melt–albedo feedback[9,41,57] and result in sea-level rise[11,58].

https://doi.org/10.1038/s41558-025-02364-4

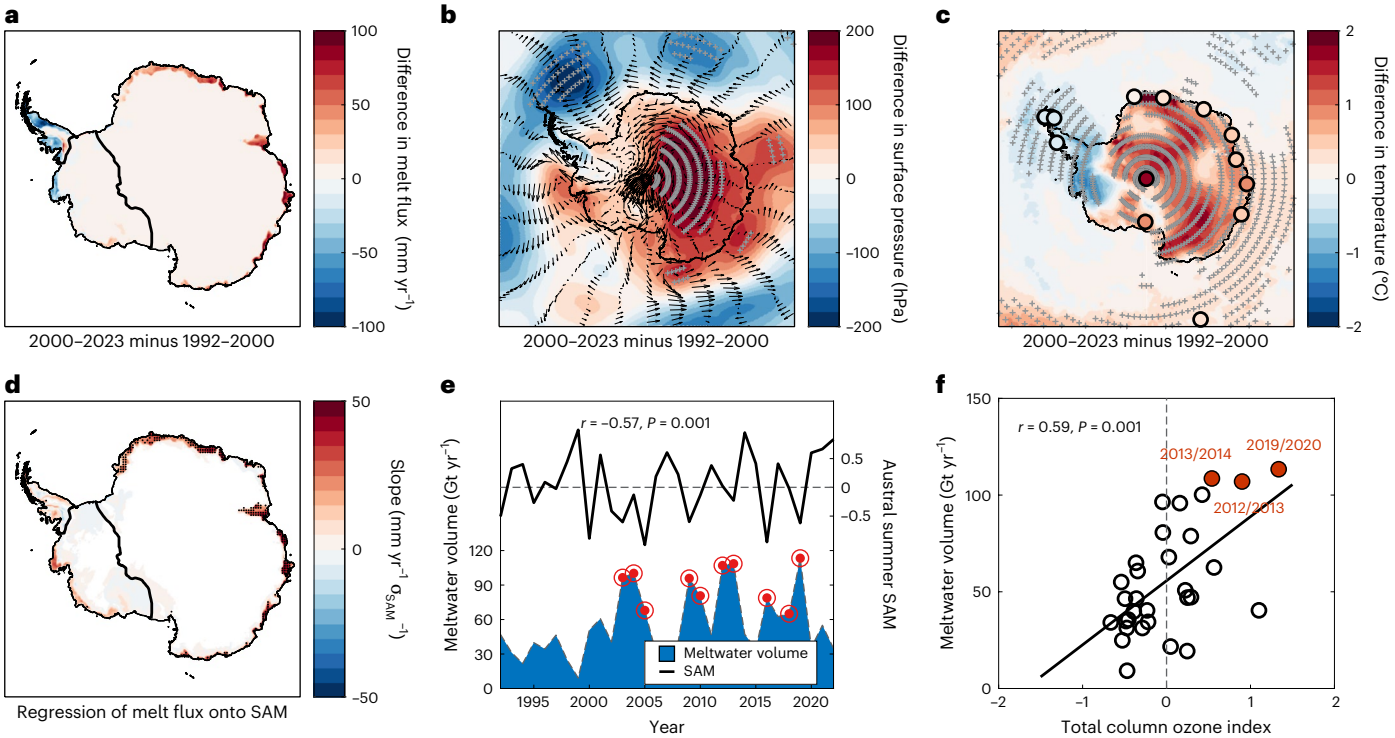

Fig. 3 | Change in AIS surface melt as a function of anomalies in atmospheric circulation. a, Difference in AIS melt flux between the 2000–2023 and 1992–2000 periods. **b**, Difference in ERA5 surface pressure and wind field between 2000–2023 and 1992–2000. **c**, Difference in austral summer (December to February) mean ERA5 air temperature between 2000–2023 and 1992–2000. Coloured dots represent temperature differences collected by Reference Antarctic Data for Environmental Research[77]. Grey pluses in **b** and **c** indicate the differences exceed 0.5 times the s.d. of the annual means. **d**, AIS annual melt flux regressed on austral summer SAM. Note that the sign of SAM is reversed. Black dots indicate the correlations are significant at a 99% confidence level. **e**, Comparison between East Antarctic annual meltwater volume and austral summer SAM. Red circles indicate the ten highest East Antarctica meltwater volume records. **f**, Scatterplot showing the comparison between total column ozone index and East Antarctica meltwater volume. Red dots represent the three years with the highest melt records. Significance of the correlation is calculated from a two-tailed *t*-test. Black lines in **a** and **d** show the boundaries between the Antarctic Peninsula, West Antarctica and East Antarctica[73].

Extreme melt favoured by the recovery of Antarctic ozone hole

The observed decrease in meltwater volume on the Antarctic Peninsula, along with the increase in East Antarctica (Figs. 1f and 3a), aligns with the reversal of the climate pattern known as 'West-warming East-cooling' since 2000, which was linked to variability in tropical sea surface temperature through tropical–polar teleconnections[59]. Reduced austral summer surface pressure in the northern Weddell Sea intensified east-to-southeasterly cold winds moving toward the Antarctic Peninsula (Fig. 3b). The cooling effect was further amplified by the increased advection of coastal sea-ice[60]. Concurrently, the increase in pressure over the Antarctic Plateau and along the coasts of the Indian and the Pacific oceans collectively contributed to the transport of warm marine air currents into East Antarctica (Fig. 3b). Consequently, austral summer mean air temperature during 2000 to 2023 has risen by up to 2 °C compared with that during 1992 to 2000 in Dronning Maud Land, where meltwater production had the highest rate of increase (Figs. 1f and 3c).

Close connections ($P < 0.05$) are found between AIS surface meltwater volume and El Niño/Southern Oscillation (Supplementary Text 3). AIS melt extent has been documented to be strongly anti-correlated with the Southern Annular Mode (SAM)[61,62], which represents the zonal pressure difference between mid and high latitudes[63]. Our regression analysis suggests the linkage between meltwater and the SAM is particularly significant and pronounced in East Antarctica (Fig. 3d and Extended Data Fig. 5b), where the record high years were almost all accompanied by a negative phase of the SAM (Fig. 3e). We show that the East Antarctic meltwater volume was also significantly correlated with the total column ozone index (TCOI, normalized October column ozone south of 60° S) ($r = 0.59$, $P < 0.01$). The three years with the highest melt in East Antarctica all occurred in the 2010s and corresponded to positive anomalies in TCOI (Fig. 3f). Meltwater produced in East Antarctica reached a maximum in 2019/2020, coinciding with the ozone hole reaching its smallest size in the last three decades (Extended Data Fig. 7).

Our finding confirms the connection between the strengthening of the SAM and the ozone recovery after 2000[64,65]. It appears that the recent recovery of the Antarctic ozone hole has favoured extreme melt events in East Antarctica associated with a negative SAM. Some ice shelves in East Antarctica showed a significant increase in meltwater volume, such as the Roi Baudouin Ice Shelf (0.07 ± 0.07 Gt yr^{-2}, $P < 0.05$). Melt fluxes for ice shelves outside the Antarctic Peninsula are still below the threshold value (725 mm w.e. yr^{-1})[33], which previously led to a significant collapse event (Extended Data Fig. 1e and Supplementary Video 1). The intensification of surface melt and rising frequency of atmospheric warming records[66,67] underline the increased importance of a focus on hydrology over East Antarctic ice shelves where extensive active surface and even subsurface meltwater were recently observed[5,34,68–71].

Conclusions

This study provides a long-term estimate of daily meltwater production from polar ice sheets using spaceborne radiometer observations. Satellites observed rapid increases in surface meltwater production over the ice sheets and ice shelves of Greenland and East Antarctica. Our analysis shows that the relationship between the NAO and

meltwater is mainly observed in northern Greenland. Accelerated surface melt in western Greenland was strongly correlated with the loss of sea-ice in Baffin Bay, which increased downward long-wave radiation. We document a notable shift in Antarctic meltwater distribution during the twenty-first century, with East Antarctica surpassing the Antarctic Peninsula as the dominant contributor to AIS meltwater production, partially attributed to the recent recovery of the Antarctic ozone hole. Large interannual variability and regional differences in meltwater production reveal a complex forcing of the surface melt climate, underlining the importance of these data for the prediction of melt-induced hydrofracture of ice shelves and ice sheet stability.

Online content

Any methods, additional references, Nature Portfolio reporting summaries, source data, extended data, supplementary information, acknowledgements, peer review information; details of author contributions and competing interests; and statements of data and code availability are available at https://doi.org/10.1038/s41558-025-02364-4.

References

1. The IMBIE team. Mass balance of the Antarctic ice sheet from 1992 to 2017. *Nature* **558**, 219–222 (2018).
2. The IMBIE team. Mass balance of the Greenland ice sheet from 1992 to 2018. *Nature* **579**, 233–239 (2020).
3. Otosaka, I. N. et al. Mass balance of the Greenland and Antarctic ice sheets from 1992 to 2020. *Earth Syst. Sci. Data* **15**, 1597–1616 (2023).
4. Jakobs, C. L., Reijmer, C. H., Kuipers Munneke, P., König-Langlo, G. & van den Broeke, M. R. Quantifying the snowmelt–albedo feedback at Neumayer Station, East Antarctica. *Cryosphere* **13**, 1473–1485 (2019).
5. Lenaerts, J. T. M. et al. Meltwater produced by wind–albedo interaction stored in an East Antarctic ice shelf. *Nat. Clim. Change* **7**, 58–62 (2017).
6. Zhang, B., Wang, Z., An, J., Liu, T. & Geng, H. A 30-year monthly 5 km gridded surface elevation time series for the Greenland ice sheet from multiple satellite radar altimeters. *Earth Syst. Sci. Data* **14**, 973–989 (2022).
7. Sole, A., Payne, T., Bamber, J., Nienow, P. & Krabill, W. Testing hypotheses of the cause of peripheral thinning of the Greenland ice sheet: is land-terminating ice thinning at anomalously high rates? *Cryosphere* **2**, 205–218 (2008).
8. Beckmann, J. & Winkelmann, R. Effects of extreme melt events on ice flow and sea level rise of the Greenland ice sheet. *Cryosphere* **17**, 3083–3099 (2023).
9. Ryan, J. C. et al. Greenland ice sheet surface melt amplified by snowline migration and bare ice exposure. *Sci. Adv.* **5**, eaav3738 (2019).
10. Leeson, A. A. et al. Supraglacial lakes on the Greenland ice sheet advance inland under warming climate. *Nat. Clim. Change* **5**, 51–55 (2015).
11. Flowers, G. E. Hydrology and the future of the Greenland ice sheet. *Nat. Commun.* **9**, 2729 (2018).
12. Cooley, S. W. & Christoffersen, P. Observation bias correction reveals more rapidly draining lakes on the Greenland ice sheet. *J. Geophys. Res. Earth Surf.* **122**, 1867–1881 (2017).
13. Boghosian, A. L. et al. Development of ice-shelf estuaries promotes fractures and calving. *Nat. Geosci.* **14**, 899–905 (2021).
14. Macdonald, G. J., Banwell, A. F. & MacAyeal, D. R. Seasonal evolution of supraglacial lakes on a floating ice tongue, Petermann Glacier, Greenland. *Ann. Glaciol.* **59**, 56–65 (2018).
15. Zwally, H. J. et al. Surface melt-induced acceleration of Greenland ice-sheet flow. *Science* **297**, 218–222 (2002).
16. Hoffman, M. J. et al. Greenland subglacial drainage evolution regulated by weakly connected regions of the bed. *Nat. Commun.* **7**, 13903 (2016).
17. Sundal, A. V. et al. Melt-induced speed-up of Greenland ice sheet offset by efficient subglacial drainage. *Nature* **469**, 521–524 (2011).
18. Pitcher, L. H. et al. Direct observation of winter meltwater drainage from the Greenland ice sheet. *Geophys. Res. Lett.* **47**, e2019GL086521 (2020).
19. Chu, V. W. Greenland ice sheet hydrology: a review. *Prog. Phys. Geogr.* **38**, 19–54 (2014).
20. van Wessem, J. M. et al. Modelling the climate and surface mass balance of polar ice sheets using RACMO2 – part 2: Antarctica (1979–2016). *Cryosphere* **12**, 1479–1498 (2018).
21. Medley, B., Neumann, T. A., Zwally, H. J., Smith, B. E. & Stevens, C. M. Simulations of firn processes over the Greenland and Antarctic ice sheets: 1980–2021. *Cryosphere* **16**, 3971–4011 (2022).
22. Banwell, A. F., Willis, I. C., Macdonald, G. J., Goodsell, B. & MacAyeal, D. R. Direct measurements of ice-shelf flexure caused by surface meltwater ponding and drainage. *Nat. Commun.* **10**, 730 (2019).
23. Banwell, A. F., Willis, I. C., Stevens, L. A., Dell, R. L. & MacAyeal, D. R. Observed meltwater-induced flexure and fracture at a doline on George VI Ice Shelf, Antarctica. *J. Glaciol.* **7**, e47 (2024).
24. Dell, R. L., Willis, I. C., Arnold, N. S., Banwell, A. F. & Husman, S. D. R. Substantial contribution of slush to meltwater area across Antarctic ice shelves. *Nat. Geosci.* **17**, 624–630 (2024).
25. Lai, C. Y. et al. Vulnerability of Antarctica's ice shelves to meltwater-driven fracture. *Nature* **584**, 574–578 (2020).
26. Alley, K. E., Scambos, T. A., Miller, J. Z., Long, D. G. & MacFerrin, M. Quantifying vulnerability of Antarctic ice shelves to hydrofracture using microwave scattering properties. *Remote Sens. Environ.* **210**, 297–306 (2018).
27. Scambos, T. et al. Ice shelf disintegration by plate bending and hydro-fracture: satellite observations and model results of the 2008 Wilkins ice shelf break-ups. *Earth Planet. Sci. Lett.* **280**, 51–60 (2009).
28. Scambos, T. A., Hulbe, C., Fahnestock, M. & Bohlander, J. The link between climate warming and break-up of ice shelves in the Antarctic Peninsula. *J. Glaciol.* **46**, 516–530 (2000).
29. Banwell, A. F. et al. The 32-year record-high surface melt in 2019/2020 on the northern George VI ice shelf, Antarctic Peninsula. *Cryosphere* **15**, 909–925 (2021).
30. Banwell, A. F., MacAyeal, D. R. & Sergienko, O. V. Breakup of the Larsen B ice shelf triggered by chain reaction drainage of supraglacial lakes. *Geophys. Res. Lett.* **40**, 5872–5876 (2013).
31. Rignot, E. et al. Accelerated ice discharge from the Antarctic Peninsula following the collapse of Larsen B ice shelf. *Geophys. Res. Lett.* **31**, L18401 (2004).
32. Christie, F. D. W. et al. Antarctic ice-shelf advance driven by anomalous atmospheric and sea-ice circulation. *Nat. Geosci.* **15**, 356–362 (2022).
33. Trusel, L. D. et al. Divergent trajectories of Antarctic surface melt under two twenty-first-century climate scenarios. *Nat. Geosci.* **8**, 927–932 (2015).
34. Bell, R. E., Banwell, A. F., Trusel, L. D. & Kingslake, J. Antarctic surface hydrology and impacts on ice-sheet mass balance. *Nat. Clim. Change* **8**, 1044–1052 (2018).
35. Zheng, L., Zhou, C. & Wang, K. Enhanced winter snowmelt in the Antarctic Peninsula: automatic snowmelt identification from radar scatterometer. *Remote Sens. Environ.* **246**, 111835 (2020).
36. Trusel, L. D., Frey, K. E., Das, S. B., Munneke, P. K. & van den Broeke, M. R. Satellite-based estimates of Antarctic surface meltwater fluxes. *Geophys. Res. Lett.* **40**, 6148–6153 (2013).
37. Colosio, P., Tedesco, M., Fettweis, X. & Ranzi, R. Surface melting over the Greenland ice sheet from enhanced resolution passive microwave brightness temperatures (1979–2019). *Cryosphere* **15**, 2623–2646 (2021).

38. Johnson, A., Hock, R. & Fahnestock, M. Spatial variability and regional trends of Antarctic ice shelf surface melt duration over 1979–2020 derived from passive microwave data. *J. Glaciol.* **68**, 533–546 (2022).
39. Banwell, A. F., Wever, N., Dunmire, D. & Picard, G. Quantifying Antarctic-wide ice-shelf surface melt volume using microwave and firn model data: 1980 to 2021. *Geophys. Res. Lett.* **50**, e2023GL102744 (2023).
40. Fettweis, X. et al. Reconstructions of the 1900–2015 Greenland ice sheet surface mass balance using the regional climate MAR model. *Cryosphere* **11**, 1015–1033 (2017).
41. Noël, B., van de Berg, W. J., Lhermitte, S. & van den Broeke, M. R. Rapid ablation zone expansion amplifies north Greenland mass loss. *Sci. Adv.* **5**, 2–11 (2019).
42. Noël, B. et al. Higher Antarctic ice sheet accumulation and surface melt rates revealed at 2 km resolution. *Nat. Commun.* **14**, 7949 (2023).
43. Zheng, L., Zhou, C. & Liang, Q. Variations in Antarctic Peninsula snow liquid water during 1999–2017 revealed by merging radiometer, scatterometer and model estimations. *Remote Sens. Environ.* **232**, 111219 (2019).
44. Smith, L. C. et al. Direct measurements of meltwater runoff on the Greenland ice sheet surface. *Proc. Natl Acad. Sci. USA* **114**, E10622–E10631 (2017).
45. Tedesco, M. Snowmelt detection over the Greenland ice sheet from SSM/I brightness temperature daily variations. *Geophys. Res. Lett.* **34**, L02504 (2007).
46. Barrand, N. E. et al. Trends in Antarctic Peninsula surface melting conditions from observations and regional climate modeling. *J. Geophys. Res. Earth Surf.* **118**, 315–330 (2013).
47. Colliander, A. et al. Ice sheet surface and subsurface melt water discrimination using multi-frequency microwave radiometry. *Geophys. Res. Lett.* **49**, e2021GL096599 (2022).
48. Zheng, L. et al. Greenland ice sheet daily surface melt flux observed from space. *Geophys. Res. Lett.* **49**, e2021GL096690 (2022).
49. Hanna, E. et al. Increased runoff from melt from the Greenland ice sheet: a response to global warming. *J. Clim.* **21**, 331–341 (2008).
50. Woollings, T. J., Hoskins, B., Blackburn, M. & Berrisford, P. A new Rossby wave-breaking interpretation of the North Atlantic Oscillation. *J. Atmos. Sci.* **65**, 609–626 (2008).
51. Hanna, E. et al. Greenland surface air temperature changes from 1981 to 2019 and implications for ice-sheet melt and mass-balance change. *Int. J. Climatol.* **41**, E1336–E1352 (2021).
52. Sellevold, R., Lenaerts, J. T. M. & Vizcaino, M. Influence of Arctic sea-ice loss on the Greenland ice sheet climate. *Clim. Dynam.* **58**, 179–193 (2021).
53. Bliss, A. C., Steele, M., Peng, G., Meier, W. N. & Dickinson, S. Regional variability of Arctic sea ice seasonal change climate indicators from a passive microwave climate data record. *Environ. Res. Lett.* **14**, 045003 (2019).
54. Preece, J. R., Wachowicz, L. J., Mote, T. L., Tedesco, M. & Fettweis, X. Summer Greenland blocking diversity and its impact on the surface mass balance of the Greenland ice sheet. *J. Geophys. Res. Atmos.* **127**, e2021JD035489 (2022).
55. Liu, J. et al. Has Arctic sea ice loss contributed to increased surface melting of the Greenland ice sheet? *J. Clim.* **29**, 3373–3386 (2016).
56. Stroeve, J. C. et al. Investigating the local-scale influence of sea ice on Greenland surface melt. *Cryosphere* **11**, 2363–2381 (2017).
57. Rennermalm, A. K. et al. Understanding Greenland ice sheet hydrology using an integrated multi-scale approach. *Environ. Res. Lett.* **8**, 015017 (2013).
58. Dirscherl, M., Dietz, A. J., Kneisel, C. & Kuenzer, C. A novel method for automated supraglacial lake mapping in Antarctica using Sentinel-1 SAR imagery and deep learning. *Remote Sens.* **13**, 197 (2021).
59. Xin, M. et al. West-warming East-cooling trend over Antarctica reversed since early 21st century driven by large-scale circulation variation. *Environ. Res. Lett.* **18**, 064034 (2023).
60. Turner, J. et al. Absence of 21st century warming on Antarctic Peninsula consistent with natural variability. *Nature* **535**, 411–415 (2016).
61. Zheng, L., Zhou, C., Zhang, T., Liang, Q. & Wang, K. Recent changes in pan-Antarctic surface snowmelt detected by AMSR-E and AMSR2. *Cryosphere* **14**, 3811–3827 (2020).
62. Tedesco, M. & Monaghan, A. J. An updated Antarctic melt record through 2009 and its linkages to high-latitude and tropical climate variability. *Geophys. Res. Lett.* **36**, L18502 (2009).
63. Marshall, G. J. Trends in the Southern Annular Mode from observations and reanalyses. *J. Clim.* **16**, 4134–4143 (2003).
64. Thompson, D. W. J. et al. Signatures of the Antarctic ozone hole in Southern Hemisphere surface climate change. *Nat. Geosci.* **4**, 741–749 (2011).
65. Banerjee, A., Fyfe, J. C., Polvani, L. M., Waugh, D. & Chang, K. L. A pause in Southern Hemisphere circulation trends due to the Montreal Protocol. *Nature* **579**, 544–548 (2020).
66. Wang, S. et al. New record of explosive warmings in East Antarctica. *Sci. Bull.* **68**, 129–132 (2022).
67. Wille, J. D. et al. The extraordinary March 2022 East Antarctica 'heat' wave. Part I: observations and meteorological drivers. *J. Clim.* **37**, 757–778 (2024).
68. Kingslake, J., Ely, J. C., Das, I. & Bell, R. E. Widespread movement of meltwater onto and across Antarctic ice shelves. *Nature* **544**, 349–352 (2017).
69. Moussavi, M. et al. Antarctic supraglacial lake detection using Landsat 8 and Sentinel-2 imagery: towards continental generation of lake volumes. *Remote Sens.* **12**, 134 (2020).
70. Arthur, J. F. et al. Large interannual variability in supraglacial lakes around East Antarctica. *Nat. Commun.* **13**, 1711 (2022).
71. Dunmire, D. et al. Observations of buried lake drainage on the Antarctic ice sheet. *Geophys. Res. Lett.* **47**, e2020GL087970 (2020).
72. Rignot, E. & Mouginot, J. Ice flow in Greenland for the International Polar Year 2008–2009. *Geophys. Res. Lett.* **39**, L11501 (2012).
73. Zwally, H. J., Giovinetto, M. B., Beckley, M. A. & Saba, J. L. Antarctic and Greenland drainage systems. *GSFC Cryospheric Sciences Laboratory* https://earth.gsfc.nasa.gov/cryo/data/polar-altimetry/antarctic-and-greenland-drainage-systems (2012).
74. Cappelen, J. Weather observations from Greenland 1958–2016: observation data with description. *DMI* www.dmi.dk/publikationer (2017).
75. Cavalieri, D. J., Parkinson, C. L. & Zwally, H. J. *Arctic and Antarctic Sea Ice Concentrations from Multichannel Passive-Microwave Satellite Data Sets: User's Guide* (Goddard Space Flight Center, 1997).
76. Hersbach, H. et al. The ERA5 global reanalysis. *Q. J. R. Meteorol. Soc.* **146**, 1999–2049 (2020).
77. Turner, J. et al. The SCAR READER project: toward a high-quality database of mean Antarctic meteorological observations. *J. Clim.* **17**, 2890–2898 (2004).

Methods

Spaceborne enhanced-resolution brightness temperatures

This study uses the calibrated enhanced-resolution passive microwave brightness temperatures (Tb) records from the NASA Making Earth System Data Records for Use in Research Environments (MEaSUREs) project. Data collected by the Defense Meteorological Satellite Program (DMSP) Special Sensor Microwave Imager (SSM/I) and the Special Sensor Microwave Imager/Sounder (SSMI/S) are used to achieve a historical passive microwave dataset. A spatial resolution enhancement algorithm is used to reconstruct coarse-resolution satellite observations on a higher spatial resolution grid[78], allowing for the investigation of detailed melt patterns that cannot be described by the coarse-resolution historical dataset[37]. Tb records at K-band (19.35 GHz) and Ka-band (37.0 GHz) provided by the National Snow and Ice Data Center (NSIDC, www.nsidc.org) are used to estimate surface melt flux. The 6.25 km Ka-band observations are interpolated to the 3.125 km Equal-Area Scalable Earth Grid (EASE-Grid). Tb records are abbreviated in this paper, with subscript E and M representing the evening and morning passes, and subscript H and V indicating the horizontal and vertical polarizations, respectively.

Melt flux from automatic weather stations

In situ surface melt flux observations are required when building the satellite-based retrieval model. Surface melt flux has not been directly observed on the polar ice sheets, but can be calculated using a surface energy balance (SEB) model forced with atmospheric measurements. In this study, daily melt fluxes at 26 automatic weather stations (AWS) from Zheng et al.[48] are used to build the melt flux retrieval model over the GrIS. Similarly, the in situ Antarctic surface melt rates at 16 AWS are used to build the melt flux retrieval model over the AIS (Supplementary Text 4).

Melt flux (M, mm w.e. day^{-1}) is calculated based on the SEB equation, with $M > 0$ only when the surface temperature (T_s) reaches the melting point:

$$M = \frac{(R_{net} + Q_s + Q_l + Q_g)\,\Delta t}{L_f \rho_w}, \text{if } T_s \geq 0\,^{\circ}\text{C} \quad (1)$$

where Δt is the model time step, L_f is the latent heat of fusion (0.334×10^6 J kg^{-1}) and ρ_w is the meltwater density (1,000 kg m^{-3}). R_{net} is the net radiation flux including both short- and long-wave components. Q_s, Q_l and Q_g represent turbulent sensible, latent and conductive subsurface heat fluxes, respectively. Radiation fluxes are provided by all the used AWS. The calculation of turbulent and conductive heat fluxes is categorized into three strategies depending on the accessibility of AWS observations (Supplementary Text 4).

Auxiliary datasets

The Tb observations are clipped using the ice edge derived from the MEaSUREs MODIS Mosaic of Greenland[79] and Antarctic coastlines obtained from the Antarctic Digital Database of the Scientific Committee on Antarctic Research. Drainage basins over the GrIS and AIS are determined according to the definitions of Rignot and Mouginot[72] and Zwally et al.[73], respectively. The GrIS melt flux retrieval model uses surface elevation data from the Greenland Ice Mapping Project[80]. Meltwater volume from satellite observations is compared with that simulated by two RCMs forced with ERA5, that is the Modèle Atmosphérique Régional (MAR)[40,81] and the Regional Atmospheric Climate Model (RACMO2.3p2) (refs. 20,41,82). The latter has been statistically downscaled from 5.5 km to 1 km for the GrIS[41] and from 27 km to 2 km for the AIS[42] to improve the surface mass balance representation, which are both used here.

Correlation and regression analyses are performed to investigate the impact of climatic drivers on increased ice sheet meltwater production. Arctic Oscillation, North Atlantic Oscillation, Greenland Blocking Index and Nino 3.4 are from the National Oceanic and Atmospheric Administration (NOAA; https://www.noaa.gov/). Atlantic Multi-decadal Oscillation is available at the National Center for Atmospheric Research[83]. The Southern Oscillation Index is derived from the pressure difference between Tahiti and Darwin Stations[84]. The SAM is calculated using the zonal pressure difference between 40° S and 65° S (ref. 63). Global surface temperature is obtained from the Met Office Hadley Centre/Climatic Research Unit global surface temperature anomalies (HadCRUT5) (refs. 85,86). The surface pressure (SP) over the Weddell Sea (80–50° S, 60° W–60° E) and the TCOI are calculated using the ERA5 climate reanalysis[76]. Sea-ice extent and concentration data are provided by the National Snow and Ice Data Center[75].

Intercalibration of Tb records from different platforms

The temporal continuity of the Tb records is affected by the updating or replacement of passive microwave sensors or satellite platforms. Despite prior adjustments to the instruments[87], substantial local Tb offsets over both ice sheets were identified, which are significant for quantitative remote sensing. To obtain a long time series of melt volume, an intercalibration process is applied to standardize the Tb observations across different platforms. Intercalibration over both ice sheets is conducted between Tb observed by DMSP SSM/I-F11, DMSP SSM/I-F13, DMSP SSMIS-F16, DMSP SSMIS-F17 and DMSP SSMIS-F18 sensors with overlaps for at least one year, and included a complete cycle of melting and refreezing. SSM/I sensors on earlier platforms are excluded from this study because DMSP-F10 exhibited significant variations in the earth incidence angle due to its orbital eccentricity, and the overlapping observation period between DMSP-F11 and DMSP-F08 is very short, lasting less than two months. Most of the AWS observations were taken during the operation period of DMSP-F17 which is therefore set as the calibration reference. The intercalibration is conducted by calculating individual slopes (m) and intercepts (n) within the overlapping periods based on a linear regression following Colosio et al.[37]:

$$\mathrm{Tb}_{cal} = m\mathrm{Tb}_{ob} + n \quad (2)$$

where Tb_{cal} and Tb_{ob} are the calibrated and observed Tb, respectively. The regression coefficients in intercalibration are listed in Extended Data Table 1.

Determination of daily freeze/thaw status

Determination of daily ice sheet surface freeze/thaw status is a prerequisite for the estimation of melt flux. A melting snowpack shows higher Tb values compared to that of a dry snowpack. Tedesco[88] and Colosio et al.[37] have proposed a dynamic algorithm that shows the best performance in melt detection when compared with the outputs from AWS and the regional climate model. In this algorithm, the surface melt is determined when the horizontally polarized Tb at 37 GHz (Tb_{37H}) exceeds the mean winter value (Tb_{winter}) plus an additional value ΔT. The idealized ΔT can be described as a function of Tb_{winter} (ref. 88):

$$\mathrm{Tb}_{37H} > \mathrm{Tb}_{winter} + \Delta T \quad (3)$$

and

$$\Delta T = a\mathrm{Tb}_{winter} + b \quad (4)$$

Based on an ensemble of microwave emission model simulations with varying snow parameters, the surface melt can be determined with $a = -0.52$ and $b = 128$ K over both Greenland and Antarctica[37,88].

Estimation of daily melt flux from spaceborne radiometer

In the absence of direct in situ melt flux measurements, we use melt fluxes derived from SEB modelling applied to AWS observations, and

regard these as ground truth when developing the satellite-based melt flux retrieval model. Recently, Zheng et al.[48] developed a method that can quantitatively estimate daily surface melt flux over the GrIS based on AWS measurements and spaceborne passive microwave observations with a machine learning model. Melt fluxes are estimated from SEB modelling based on 26 GrIS AWS observations (14,647 samples in total), which are separated into training (70%), validation (15%) and test (15%) collections. The melt flux retrieval model was established based on a nonlinear back-propagation neural network (BNN) architecture, with inputs consisting of K- and Ka-bands Tb at both polarizations (horizontal and vertical) and passes (morning and evening), surface elevation and day of the melting year (DOY, 1 January to 31 December for the GrIS). The BNN architecture makes the adjusted network capable of getting the desired output, as each unit in the hidden layer receives an 'error feedback' connection that modifies the weights between the neurons[89]. The optimal BNN model shows a root mean square error of 9.3 mm w.e. day^{-1} and r of 0.83 over the GrIS on independent testing collection[48].

The BNN model does not perform well when applied to the AIS. This is because many fewer in situ measurements (3,619 samples from 16 AWS in total) are available for model training over a much larger ice sheet with a shorter melt season. Overfitting may occur in neural networks with small sample sizes for training. Instead, the support vector regression (SVR) is used to estimate daily meltwater production over the AIS. The SVR model is trained based on the risk minimization principle in statistical learning[90], and can prevent overfitting even when dealing with few data in very high-dimensional spaces[91]. SVR transforms the input vector ($\mathbf{X}$) into a high-dimensional feature space by using a kernel function $\mathbf{\Phi}$ that can describe nonlinear relationships:

$$M = \mathbf{W}^{\mathrm{T}}\Phi(\mathbf{X}) + b, \text{with } \mathbf{X} = [\mathrm{Tb}_{\mathrm{E19V}}, \mathrm{Tb}_{\mathrm{M19V}}, \mathrm{Tb}_{\mathrm{E19H}}, \mathrm{Tb}_{\mathrm{M19H}}, \mathrm{Tb}_{\mathrm{E37V}}, \mathrm{Tb}_{\mathrm{M37V}}, \mathrm{Tb}_{\mathrm{E37H}}, \mathrm{Tb}_{\mathrm{M37H}}, \mathrm{DOY}] \quad (5)$$

where $\mathbf{W}^{\mathrm{T}}$ and b are the weight vector and offset of the equation, and $\mathbf{\Phi}$ is the kernel function. The input matrix is comprised of the K- and Ka-bands Tb at both polarizations (horizontal and vertical) and passes (morning and evening), as well as DOY (1 July to 30 June for the AIS). In the training of the SVR model, 85% of the samples are employed using tenfold cross-validation. The remaining 15% of the samples are used in independent testing. A Gaussian kernel function shows the best performance in the tried-and-tested experiments, with a root mean square error of 2.45 mm w.e. day^{-1} and an r of 0.80 on the independent testing collection (Extended Data Fig. 8). To save computational resources, the SVR model is only applied at elevations below 2,000 m since melt does not typically occur at higher elevations over the AIS[92].

Uncertainties in satellite-derived melt flux stem from several sources. The resolution enhancement algorithm provides improved resolution of satellite observations at the expense of an increased noise level, but the multiple passes in polar regions allow for a low-level noise[37,78]. We acknowledge that model uncertainties may arise in regions with limited in situ melt flux data. Future expansion of in situ measurements in the north Greenland, the Wilkes and Adélie Lands in the AIS will enhance the reliability of remote sensing estimates. Apart from the melt flux retrieval model, uncertainty also stems from the observed melt flux which is regarded as ground truth in BNN and SVR model training, neglecting observational errors and the necessary simplification assumptions made in the SEB model[4,48]. Snow density changes spatially and temporally on the ice sheet, but is set to a constant value in the calculation of subsurface heat flux. Nevertheless, the effect is almost negligible because the subsurface heat flux is very small compared with other components and is sometimes ignored[48]. The coefficients used in the surface melt detection algorithm are determined based on a set of ideal model experiments for a 5 cm homogeneous snow layer with a liquid water content of 0.2%. Though this method works well for both ice sheets[37,88], melt signals may be misidentified as snow properties can certainly be much more complex. In addition, melt detection methods with a constant threshold may also miss weak melt events[35]. The calving fronts of the Antarctic ice shelves and Greenland outlet glaciers could also lead to great variations in Tb, which may be mistaken for melt events and disturb melt flux estimation.

Data availability

The SSM/I and SSMIS passive microwave observations are provided by the National Snow and Ice Data Center (https://nsidc.org/data/nsidc-0630/versions/1). AWS daily melt flux over the GrIS is available via Figshare at https://doi.org/10.6084/m9.figshare.17324009.v1 (ref. 48). The AIS benchmark AWS daily melt fluxes were provided by C. L. Jakobs[93] and the melt flux data from additional AWS are available via Figshare at https://doi.org/10.6084/m9.figshare.28052417.v2 (ref. 94). Satellite-derived melt flux and meltwater volume over both ice sheets generated in this study can be found via Figshare at https://doi.org/10.6084/m9.figshare.24310153.v1 (ref. 95).

Code availability

The MATLAB scripts used to estimate melt flux from remote sensing observations and to draw the main figures are available via Figshare at https://doi.org/10.6084/m9.figshare.25909720.v2 (ref. 96).

References

78. Long, D. G. & Daum, D. L. Spatial resolution enhancement of SSM/I data. *IEEE Trans. Geosci. Remote Sens.* **36**, 407–417 (1998).
79. Haran, T., Bohlander, J., Scambos, T., Painter, T. & Fahnestock, M. MEaSUREs MODIS Mosaic of Greenland (MOG) 2005, 2010, and 2015 Image Maps v. 2 (NASA National Snow and Ice Data Center, 2018); https://nsidc.org/data/nsidc-0547/versions/2
80. Howat, I. M., Negrete, A. & Smith, B. E. The Greenland Ice Mapping Project (GIMP) land classification and surface elevation datasets. *Cryosphere* **8**, 1509–1518 (2014).
81. Dethinne, T. et al. Sensitivity of the MAR regional climate model snowpack to the parameterization of the assimilation of satellite-derived wet-snow masks on the Antarctic Peninsula. *Cryosphere* **17**, 4267–4288 (2023).
82. Noël, B. et al. A daily, 1 km resolution data set of downscaled Greenland ice sheet surface mass balance (1958–2015). *Cryosphere* **10**, 2361–2377 (2016).
83. Schneider, D. P., Deser, C., Fasullo, J. & Trenberth, K. E. Climate data guide spurs discovery and understanding. *Eos Trans. AGU* **94**, 121–122 (2013).
84. Ropelewski, C. F. & Jones, P. D. An extension of the Tahiti–Darwin Southern Oscillation Index. *Mon. Weather Rev.* **115**, 2161–2165 (1987).
85. Morice, C. P. et al. An updated assessment of near-surface temperature change from 1850: the HadCRUT5 data set. *J. Geophys. Res. Atmos.* **126**, e2019JD032361 (2019).
86. Osborn, T. J. & Jones, P. D. The CRUTEM4 land-surface air temperature data set: construction, previous versions and dissemination via Google earth. *Earth Syst. Sci. Data* **6**, 61–68 (2014).
87. Berg, W., Kroodsma, R., Kummerow, C. D. & McKague, D. S. Fundamental climate data records of microwave brightness temperatures. *Remote Sens.* **10**, 1306 (2018).
88. Tedesco, M. Assessment and development of snowmelt retrieval algorithms over Antarctica from K-band spaceborne brightness temperature (1979–2008). *Remote Sens. Environ.* **113**, 979–997 (2009).
89. Hecht-Nielsen, R. Theory of the backpropagation neural network. In *Proc. International 1989 Joint Conference on Neural Networks* 593–605 (IEEE, 1989); https://doi.org/10.1109/ijcnn.1989.118638

90. Vapnik, V., Golowich, S. E. & Smola, A. Support vector method for function approximation, regression estimation, and signal processing. In *Proc. 10th International Conference on Neural Information Processing Systems* (eds Mozer, M. C. et al.) 281–287 (1996).
91. Smola, A. J. & Schölkopf, B. A tutorial on support vector regression. *Stat. Comput.* **14**, 199–222 (2004).
92. Tedesco, M., Abdalati, W. & Zwally, H. J. Persistent surface snowmelt over Antarctica (1987–2006) from 19.35 GHz brightness temperatures. *Geophys. Res. Lett.* **34**, L18504 (2007).
93. Jakobs, C. L. et al. A benchmark dataset of in situ Antarctic surface melt rates and energy balance. *J. Glaciol.* **66**, 291–302 (2020).
94. Zheng, L. & Wu, J. Daily melt flux estimated from Antarctic automatic weather station data. *figshare* https://doi.org/10.6084/m9.figshare.28052417.v2 (2024).
95. Zheng, L. Melt flux and meltwater volume over polar ice sheets from satellite passive microwave observations. *figshare* https://doi.org/10.6084/m9.figshare.24310153.v1 (2024).
96. Zheng, L. Codes to estimate melt flux from passive microwave brightness temperature, and to display the melt distribution, trends and climatic linkages. *figshare* https://doi.org/10.6084/m9.figshare.25909720.v2 (2024).

Acknowledgements

This work was supported by the National Natural Science Foundation of China (grant nos. 42422606, 41925027 and 42006192), the Innovation Group Project of Southern Marine Science and Engineering Guangdong Laboratory (Zhuhai) (grant no. 311024008). M.R.v.d.B. acknowledges funding from the Netherlands Earth System Science Center. B.N. is a research associate of the Fonds de la Recherche Scientifique de Belgique (F.R.S.-FNRS). Computational resources for running the MAR model were provided by the Consortium des Équipements de Calcul Intensif, funded by the F.R.S.-FNRS under grant no. 2.5020.11, the Walloon Region, and the Tier-1 supercomputer (Lucia) infrastructure, funded by the Walloon Region under grant agreement no. 1910247. We thank S. Wang and B. Huai for their helpful discussion and suggestions. We also thank H. de Verteuil for the English editing.

Author contributions

L.Z. and X.C. had primary responsibility for study design. L.Z. built the melt flux retrieval models, produced the melt products, analysed the data and wrote the paper. X.S. preprocessed the passive microwave brightness temperature data and assisted in developing the methodology. M.R.v.d.B. and B.N. provided the RACMO2.3p2 dataset, and assisted in interpreting the results and revising the paper. X.L. assisted in interpreting and discussing the results. X.F. provided the MAR3.12 and MAR3.14 datasets and contributed to refining the paper. Q.L. and K.W. helped with statistical analyses. J.L. assisted in interpreting the results and revising the paper. X.C. acquired the funding and provided supervision. All authors commented on the paper.

Competing interests

The authors declare no competing interests.

Additional information

Extended data is available for this paper at https://doi.org/10.1038/s41558-025-02364-4.

Supplementary information The online version contains supplementary material available at https://doi.org/10.1038/s41558-025-02364-4.

Correspondence and requests for materials should be addressed to Xiao Cheng.

Peer review information *Nature Climate Change* thanks the anonymous reviewers for their contribution to the peer review of this work.

https://doi.org/10.1038/s41558-025-02364-4

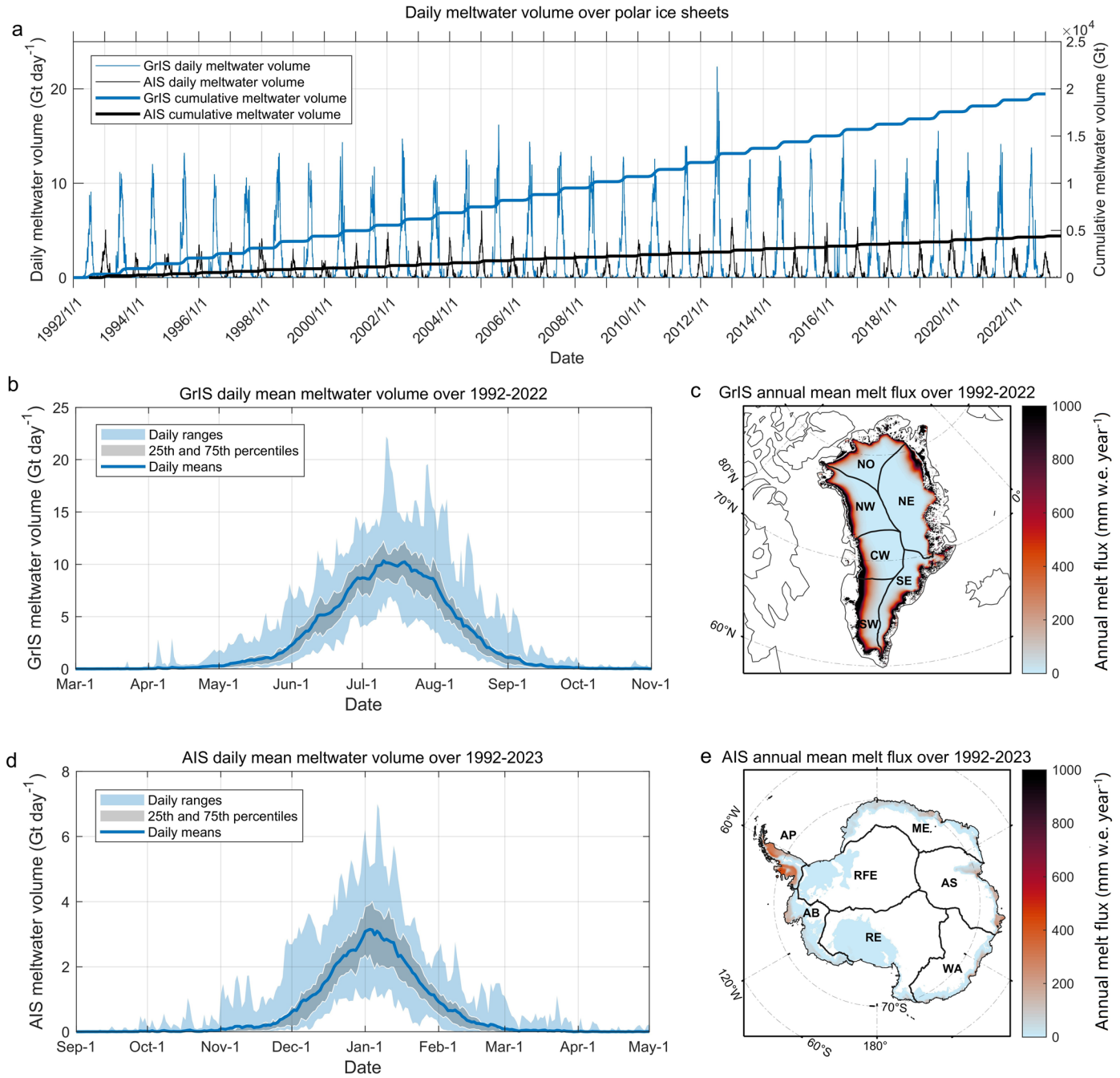

Extended Data Fig. 1 | Satellite-derived surface melt over the Greenland Ice Sheet and Antarctic Ice Sheet during 1992-2022/2023. (**a**) Daily meltwater volume and cumulative meltwater volume over the GrIS (blue lines) and AIS (black lines). (**b**) and (**d**) show daily mean meltwater volume over the GrIS and AIS, with blue shadows indicating the ranges and gray shadows indicating the 25th and 75th percentiles. (**c**) and (**e**) show maps of the annual mean surface melt rate over the GrIS and AIS, respectively. Black lines in (**c**) and (**e**) delineate the boundaries of the respective basins adopted from Rignot and Mouginot[72] and Zwally et al.[73], respectively.

https://doi.org/10.1038/s41558-025-02364-4

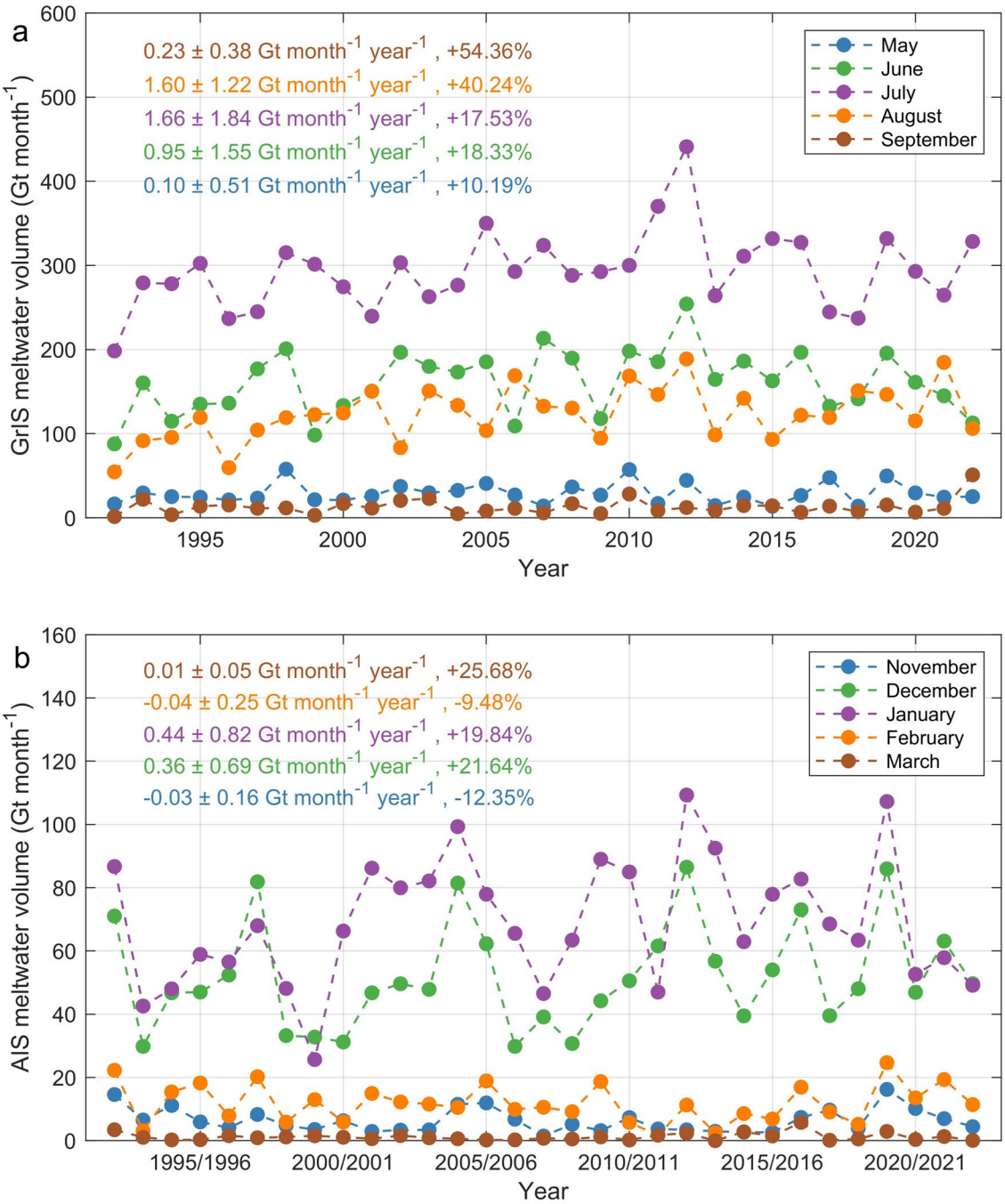

Extended Data Fig. 2 | Time series of monthly meltwater volume throughout the melt season. (**a**) and (**b**) show the statistics in Greenland and Antarctica, respectively. Uncertainties of trends are estimated at a 95% confidence level (two-tailed t-test). Relative changes are calculated by referring to the annual average over the study period.

https://doi.org/10.1038/s41558-025-02364-4

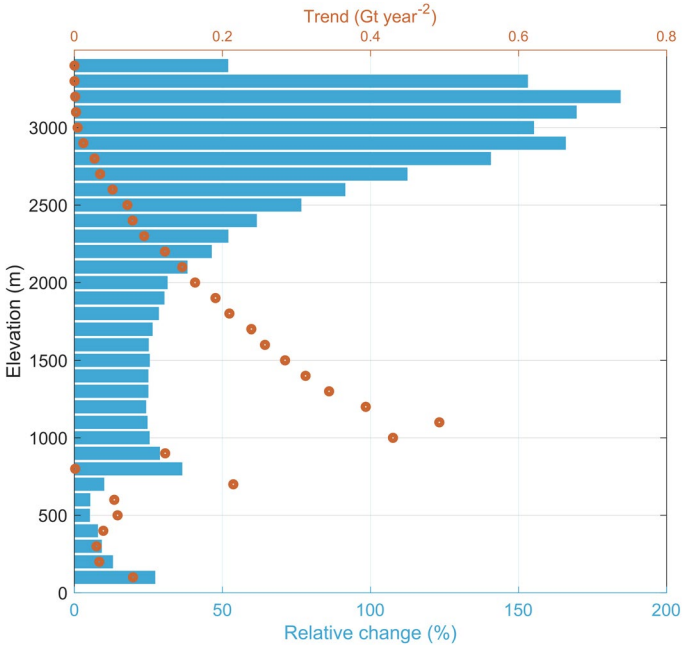

Extended Data Fig. 3 | Changes in satellite-derived Greenland annual meltwater volume at different elevations during the study period. Trend and relative change are calculated at different elevations (100 m interval) during 1992-2022. Relative change is calculated by referring to the annual average at each elevation interval.

https://doi.org/10.1038/s41558-025-02364-4

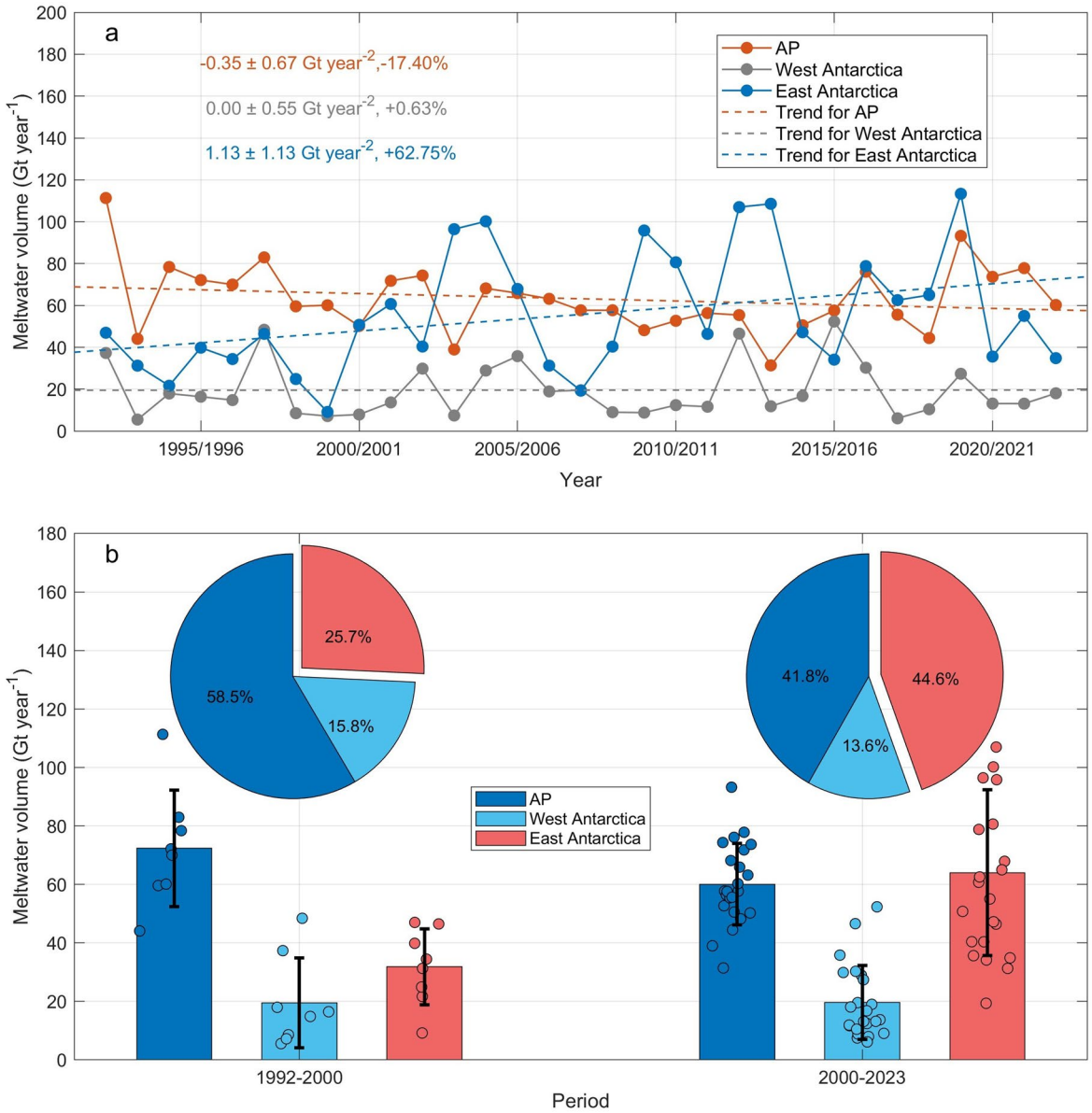

Extended Data Fig. 4 | Changes in Antarctic meltwater volume during 1992-2023. (**a**) Annual meltwater volume in Antarctic Peninsula (AP), West Antarctica and East Antarctica, as well as the corresponding trends from satellite estimates. Uncertainties of trends are estimated at a 95% confidence level (two-tailed t-test). (**b**) Means and standard deviations of annual meltwater volume during 1992-2000 (n = 8) and 2000-2023 (n = 23) and the corresponding proportion from the AP, West Antarctica and East Antarctica.

https://doi.org/10.1038/s41558-025-02364-4

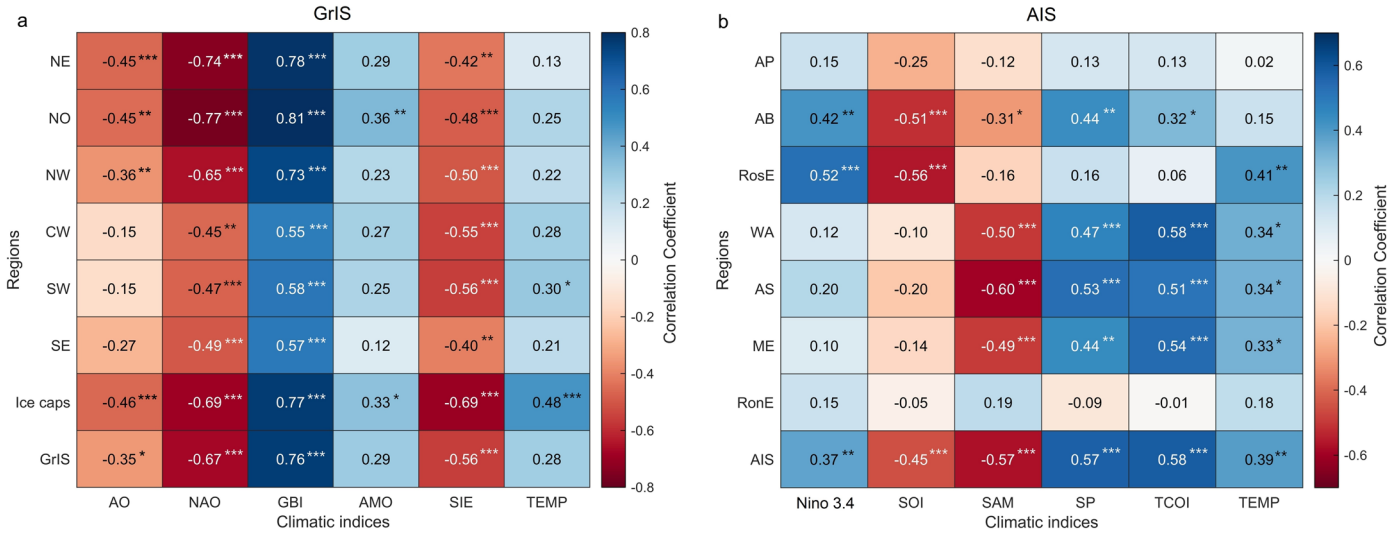

Extended Data Fig. 5 | Linkages between ice sheet meltwater volume and climate indices. (**a**) Correlations between GrIS annual meltwater volume and climate indices during 1992-2022. (**b**) Correlations between AIS annual meltwater volume and climate indices during 1992-2023. The climatic indices investigated include global surface temperature, the Arctic Oscillation (AO), North Atlantic Oscillation (NAO), Greenland Blocking Index (GBI), Atlantic Multi-decadal Oscillation (AMO), Nino 3.4, Southern Oscillation Index (SOI), South Annular Mode (SAM), surface pressure (SP) over the Weddell Sea (80°S-50°S, 60°W-60°E) and the Total Column Ozone Index (TCOI, normalized October column zone south of 60°S). Climate indices are averaged over the summer months (JJA) for the GrIS, and over the austral summer months (DJF), with the exception of the TCOI. Stars in the map indicate the correlations are significant at 90% (*), 95% (**) and 99% (***) confidence levels (two-tailed t-test).

https://doi.org/10.1038/s41558-025-02364-4

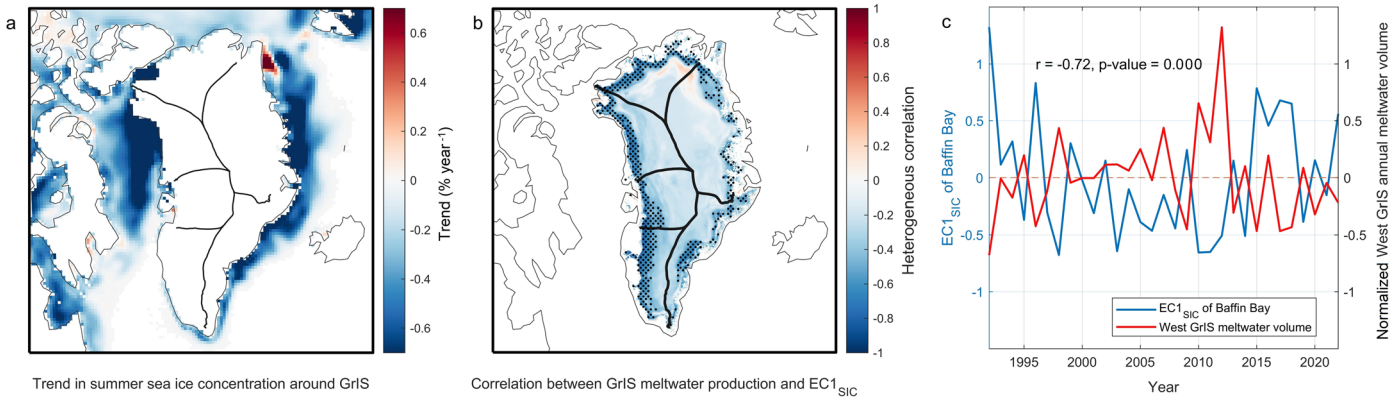

Extended Data Fig. 6 | Relation between Baffin Bay sea ice and western Greenland surface melt. Singular value decomposition (SVD) analysis between sea ice in Baffin Bay (55°N-75°N, 75°W-50°W) and surface melt in western Greenland. (**a**) Trend in summer sea ice concentration (SIC)[75] during 1992-2022. (**b**) Heterogeneous correlation between GrIS surface melt flux and the associated expansion coefficient (EC) of leading SVD mode for sea ice concentration ($EC1_{SIC}$) in Baffin Bay. Black points indicate the correlations are significant at a 99% confidence level (two-tailed t-test). Black lines are the boundaries of GrIS basins[72]. (**c**) Comparison between Baffin Bay $EC1_{SIC}$ and normalized west GrIS (including NW, CW, SW Basins) meltwater volume. Significance of the correlation is calculated from a two-tailed t-test.

https://doi.org/10.1038/s41558-025-02364-4

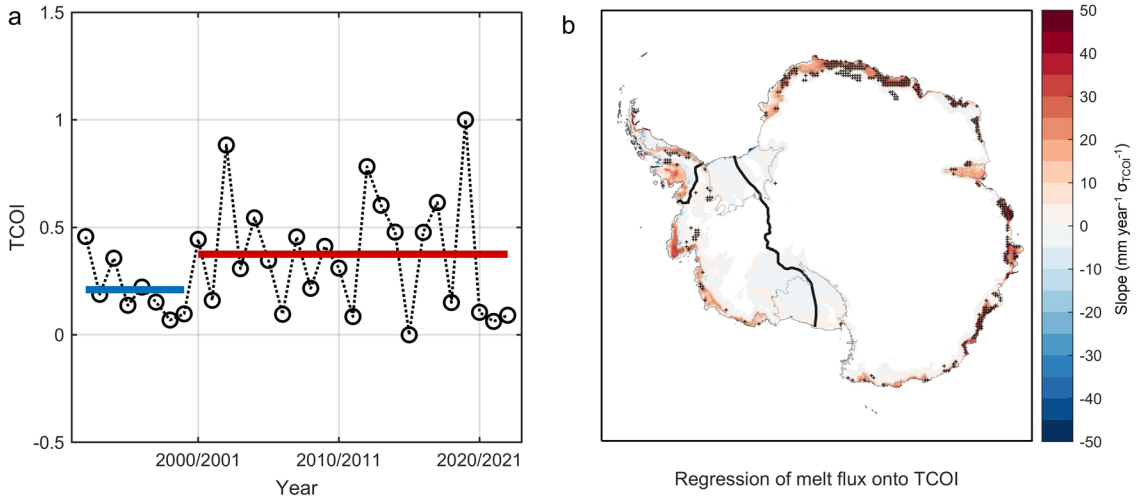

Extended Data Fig. 7 | Relation between Antarctic ozone hole and surface melt. (**a**) Time-series of TCOI during 1992-2023. Blue and red lines show the averages for 1992-2000 and 2000-2023, respectively. (**b**) Antarctic annual melt flux regressed onto TCOI. Black pluses indicate the correlations are statistically significant at a 99% confidence level (two-tailed t-test). Black lines indicate the boundaries between the Antarctic peninsula, West Antarctica and East Antarctica[73].

https://doi.org/10.1038/s41558-025-02364-4

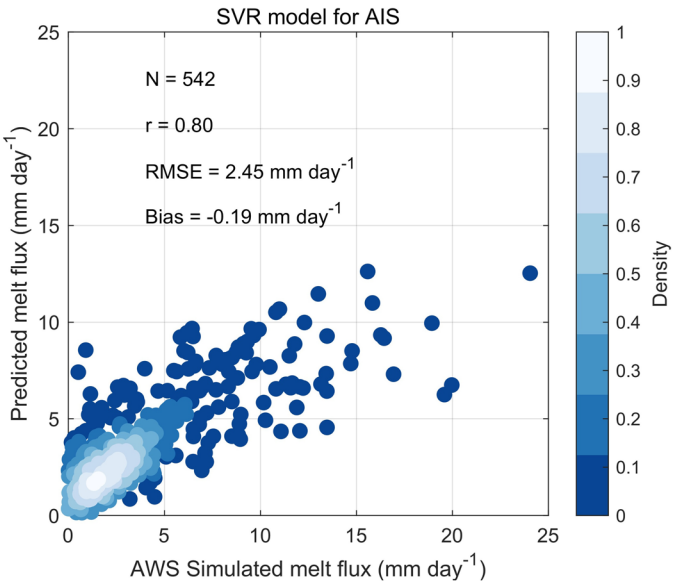

Extended Data Fig. 8 | Validation of AIS melt flux retrieval model. Comparisons between AIS daily melt flux estimated from automatic weather stations (AWS) observations with that predicted by a support vector regression (SVR) model. The validation is based on the independent testing collections (15% of the total samples).

https://doi.org/10.1038/s41558-025-02364-4

Extended Data Table 1 | Inter-calibration of Special Sensor Microwave Imager (SSM/I) and Special Sensor Microwave Imager/Sounder (SSMIS) observations

Region	Channels	SSM/I F11 to SSMIS F17		SSM/I F13 to SSMIS F17		SSMIS F16 to SSMIS F17		SSMIS F18 to SSMIS F17	
		m	*n* (K)	*m*	*n* (K)	*m*	*n* (K)	*m*	*n* (K)
GrIS	Tb_{E37H}	1.007	-1.198	0.997	0.411	0.991	0.715	0.975	2.968
	Tb_{M37H}	1.000	-0.042	0.988	1.810	0.953	6.879	0.972	3.437
	Tb_{E37V}	1.008	-2.211	0.998	-0.048	1.013	-2.758	0.995	0.230
	Tb_{M37V}	1.007	-2.362	0.996	0.118	0.973	4.931	0.996	-0.072
	Tb_{E19H}	0.992	0.663	0.989	1.084	0.998	0.621	0.985	1.715
	Tb_{M19H}	0.980	2.444	0.979	2.479	0.983	3.128	0.980	2.377
	Tb_{E19V}	0.999	-0.039	0.994	1.022	1.002	-0.629	0.996	-0.028
	Tb_{M19V}	0.993	0.953	0.990	1.704	0.983	3.042	0.993	0.513
AIS	Tb_{E37H}	1.012	-1.969	0.995	0.851	0.971	4.054	0.989	0.432
	Tb_{M37H}	0.970	5.285	0.970	5.186	0.969	4.480	0.954	6.122
	Tb_{E37V}	1.020	-4.188	1.003	-0.795	0.988	1.747	1.011	-2.720
	Tb_{M37V}	0.991	1.323	0.984	2.847	0.995	0.398	0.975	4.223
	Tb_{E19H}	0.986	2.001	0.980	2.775	0.993	1.004	0.991	0.931
	Tb_{M19H}	0.970	4.532	0.971	4.219	0.989	1.727	0.975	3.362
	Tb_{E19V}	0.991	2.038	0.982	4.050	0.994	0.539	0.999	-0.398
	Tb_{M19V}	0.974	5.747	0.970	6.678	0.991	1.208	0.983	2.857

Slopes (*m*) and intercepts (*n*) in Eq. 2 for the inter-calibration of Special Sensor Microwave Imager (SSM/I) and Special Sensor Microwave Imager/Sounder (SSMIS) observations. Note that DMSP-F17 is the calibration reference.